

Analysis of explosion wave interactions and rock breaking effects during dual initiation

Renshu Yang, Jinjing Zuo, Liwei Ma, Yong Zhao, Zhen Liu, and Quanmin Xie

Cite this article as:

Renshu Yang, Jinjing Zuo, Liwei Ma, Yong Zhao, Zhen Liu, and Quanmin Xie, Analysis of explosion wave interactions and rock breaking effects during dual initiation, *Int. J. Miner. Metall. Mater.*, 31(2024), No. 8, pp. 1788-1798. <https://doi.org/10.1007/s12613-024-2830-y>

View the article online at [SpringerLink](#) or [IJMMM Webpage](#).

Articles you may be interested in

Noora Hytönen, Zai-qing Que, Pentti Arffman, Jari Lydman, Pekka Nevasmaa, Ulla Ehrnstén, and Pål Efsing, [Effect of weld microstructure on brittle fracture initiation in the thermally-aged boiling water reactor pressure vessel head weld metal](#), *Int. J. Miner. Metall. Mater.*, 28(2021), No. 5, pp. 867-876. <https://doi.org/10.1007/s12613-020-2226-6>

Jun-peng Wang, Tao Jiang, Ya-jing Liu, and Xiang-xin Xue, [Influence of microwave treatment on grinding and dissociation characteristics of vanadium titano-magnetite](#), *Int. J. Miner. Metall. Mater.*, 26(2019), No. 2, pp. 160-167. <https://doi.org/10.1007/s12613-019-1720-1>

En-ming Zhang, Yi-ming Zhao, Zhong-mou Wang, and Wen-ya Li, [Effect of heat treatment on the microstructure and mechanical properties of structural steel–mild steel composite plates fabricated by explosion welding](#), *Int. J. Miner. Metall. Mater.*, 27(2020), No. 8, pp. 1115-1122. <https://doi.org/10.1007/s12613-020-1986-3>

Xin Chen, Mei-feng Cai, Jian-chuan Li, and Wen-hui Tan, [Theoretical analysis of JMC effect on stress wave transmission and reflection](#), *Int. J. Miner. Metall. Mater.*, 25(2018), No. 11, pp. 1237-1245. <https://doi.org/10.1007/s12613-018-1676-6>

Dong-tao Wang, Hai-tao Zhang, Lei Li, Hai-lin Wu, Ke Qin, and Jian-zhong Cui, [The evolution of microstructure and mechanical properties during high-speed direct-chill casting in different Al-Mg₂Si *in situ* composites](#), *Int. J. Miner. Metall. Mater.*, 25(2018), No. 9, pp. 1080-1089. <https://doi.org/10.1007/s12613-018-1659-7>

Wei Xiao, Yan-ping Bao, Chao Gu, Min Wang, Yu Liu, Yong-sheng Huang, and Guang-tao Sun, [Ultrahigh cycle fatigue fracture mechanism of high-quality bearing steel obtained through different deoxidation methods](#), *Int. J. Miner. Metall. Mater.*, 28(2021), No. 5, pp. 804-815. <https://doi.org/10.1007/s12613-021-2253-y>



IJMMM WeChat



QQ author group

Analysis of explosion wave interactions and rock breaking effects during dual initiation

Renshu Yang^{1,2)}, Jinjing Zuo^{1,2),✉}, Liwei Ma¹⁾, Yong Zhao^{1,2)}, Zhen Liu¹⁾, and Quanmin Xie³⁾

1) School of Civil and Resource Engineering, University of Science and Technology Beijing, Beijing 100083, China

2) Research Institute of Macro-Safety Science, University of Science and Technology Beijing, Beijing 100083, China

3) State Key Laboratory of Precision Blasting, Jiangnan University, Wuhan 430056, China

(Received: 21 November 2023; revised: 20 December 2023; accepted: 12 January 2024)

Abstract: In blasting engineering, the location and number of detonation points, to a certain degree, regulate the propagation direction of the explosion stress wave and blasting effect. Herein, we examine the explosion wave field and rock breaking effect in terms of shock wave collision, stress change of the blast hole wall in the collision zone, and crack propagation in the collision zone. The produced shock wave on the collision surface has an intensity surpassing the sum of the intensities of the two colliding explosion shock waves. At the collision location, the kinetic energy is transformed into potential energy with a reduction in particle velocity at the wave front and the wave front pressure increases. The expansion form of the superposed shock wave is dumbbell-shaped, the shock wave velocity in the collision area is greater than the radial shock wave velocity, and the average propagation angle of the explosion shock waves is approximately 60°. Accordingly, a fitted relationship between blast hole wall stress and explosion wave propagation angle in the superposition area is plotted. Under the experimental conditions, the superimposed explosion wave stress of the blast hole wall is approximately 1.73 times the single-explosion wave incident stress. The results of the model test and numerical simulations reveal that large-scale radial fracture cracks were generated on the blast hole wall in the superimposed area, and the width of the crack increased. The width of the large-scale radial fracture cracks formed by a strong impact is approximately 5% of the blast hole length. According to the characteristics of blast hole wall compression, the mean peak pressures of the strongly superimposed area are approximately 1.48 and 1.84 times those of the weakly superimposed and nonsuperimposed areas, respectively.

Keywords: blasting; shock wave collision; high-speed schlieren system; crack fracture characteristic; explosion wave

1. Introduction

Cylindrical charge blasting has a significant role in practical engineering, and the excitation stress field is the key to influence the blasting effect. The location of the detonated point influences the distribution of the explosion stress field and the final rock breaking effect. The frequently used detonated-point layouts are forward, reverse, and double-end detonations [1–4], of which double-end-detonated explosives completely explode in a shorter time than the other types. It is imperative to investigate the explosion wave process and superimposed stress field distribution of double-end-detonated explosives. The influence of the detonated-point location on the blasting effect can be explored by using small-sized model laboratory tests and numerical simulations. Zhang *et al.* [5–7] developed a multiprimer initiation blasting method based on the shock wave collision principle and used it in a field engineering scenario. They found that the problem of pillarless sublevel caving of a suspended roof can be effectively solved by multiprimer initiation. Leng *et al.* [8–9] analyzed the tension and compression shear failure zones in an

exploded medium under different initiation modes and found that the spatial distribution of the explosion energy can be adjusted by changing the number of initiation points in practical blasting engineering. Onederra *et al.* [10] coupled their developed hybrid stress blasting model with experiments and observed that the damage range of the bottom of a blast hole is significantly smaller than that of its mouth when bottom initiation is adopted. Liu *et al.* [11] independently developed a set of tension and compression damage models with finite element software and then assessed the influences of various initiation point positions on bench blasting. Gao *et al.* [12–13] investigated the crushing effects of rock at different initiation points and measured that the blasting vibration of the bottom initiation was 61.3% smaller than that of the top initiation. Miao *et al.* [14–15] proposed a novel method named the symmetric bilinear initiation system based on the shock wave collision principle, which was found to increase the effect of rock fragmentation. Haeri [16] examined the effects of crack positions on the fracturing path in the bridge areas of double-cracked beam specimens.

To explore an explosion wave field, Zuo *et al.* [17–18]

✉ Corresponding author: Jinjing Zuo E-mail: cumtbzjj@163.com

© University of Science and Technology Beijing 2024

analyzed the propagation characteristics of the explosion shock waves and gases during the end and center initiations of a cylindrical charge and found that the damage range of the medium in each initiation mode was approximately five times the blast hole diameter and analyzed the explosion wave characteristics under an eccentric decoupled charge. Yang and Zuo [19] explored the explosion wave field propagation of a shaped charge explosion, determined the evolution characteristics of the explosion shock waves in the shaped and vertical directions, and found that the intensity of the explosion shock wave in the shaped direction was 2.3 times that in the vertical-shaped direction. Gerasimovet and Trepalov [20] employed the background-oriented schlieren technique to probe the movement law of an explosion shock wave, obtained a reference to observe the propagation of an explosion shock wave in space, estimated the explosion energy, and obtained the shock wave parameters.

Herein, we built a collision principle structure diagram of two oppositely spreading explosion shock waves based on the shock wave collision characteristics and Hugoniot curves. A high-speed schlieren experiment system was utilized, a shock wave collision experiment model was constructed, and the evolution of the explosion shock waves and gas over the entire time domain was examined. A mechanics model of the role of shock wave collision with the wall of a blast hole was designed, and force characteristic analysis of the collision superposition area was conducted. A numerical simulation analysis model was built, the development processes of the effective stress and damage of a specimen were examined, and the pressure–time history curve of the blast hole wall was constructed. Generally, the contribution of this work is to explore the explosion wave field and rock breaking effect of the two ends of the detonated explosive in the blast hole in terms of shock wave collision, stress change of the hole wall in the collision zone, and crack propagation in the collision zone.

2. Shock wave collision mechanism of the explosive detonated from both ends

Fig. 1 illustrates a schematic of the collision of two shock waves, where S_1 and S_2 propagate to the left and right, respectively. Based on the stress and particle velocity on the collision surface, the stress state in the collision is related to the intersection of the P – u Hugoniot curves.

The Hugoniot curve of a shock wave can be expressed as [1,21]:

$$P = \rho_0 C_0 (u - u_0) + \rho_0 s (u - u_0) \quad (1)$$

where P refers to the pressure, C_0 refers to the sonic velocity of the medium, s refers to an empirical constant, u refers to the particle propagation velocity, u_0 refers to the initial particle propagation velocity, and ρ_0 refers to the initial density.

At initial time, $u_0 = 0$, and for shock waves S_1 and S_2 ,

$$\begin{cases} \rho_0 s u^2 + \rho_0 C_0 u - P_1 = 0 \\ \rho_0 s u^2 + \rho_0 C_0 u - P_2 = 0 \end{cases} \quad (2)$$

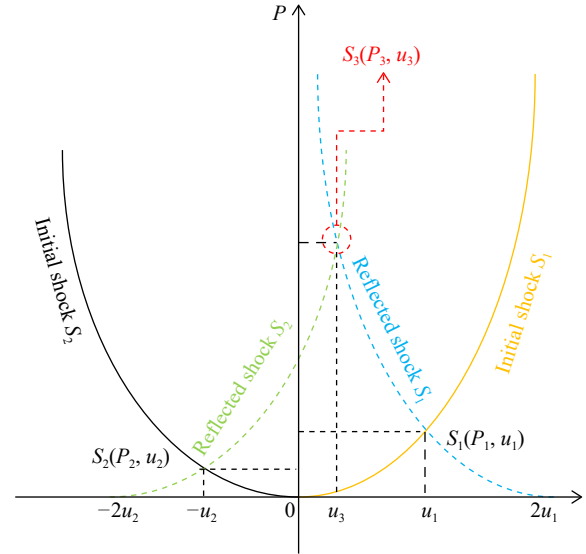


Fig. 1. Schematic of the shock wave collision. P_i refers to the pressure; u_i refers to the particle propagation velocity ($i = 1, 2, 3$).

By solving Eq. (2),

$$\begin{cases} P_1 = \rho_0 C_0 (2u_1 - u) + \rho_0 s (2u_1 - u)^2 \\ P_2 = \rho_0 C_0 (2u_2 - u) + \rho_0 s (2u_2 - u)^2 \end{cases} \quad (3)$$

When shock waves S_1 and S_2 pass through $P = 0$, Eq. (1) can be expressed as

$$\begin{cases} P_1 = \rho_0 C_0 (2u_1 - u) + \rho_0 s (2u_1 - u)^2 \\ P_2 = \rho_0 C_0 (2u_2 - u) + \rho_0 s (2u_2 - u)^2 \end{cases} \quad (4)$$

On the basis of the superposition curve, the particle propagation velocity, u_3 , at the collision intersection point is

$$u_3 = u_1 + u_2 \quad (5)$$

Substituting Eq. (5) into Eq. (4) calculates the interface pressure P_3 :

$$P_3 = \rho_0 C_0 (2u_1 - u_3) + \rho_0 s (2u_1 - u_3)^2 \quad (6)$$

$$P_3 - (P_1 + P_2) = 2\rho_0 u_2 (C_0 + s u_1) \quad (7)$$

Based on Eq. (3), $u_2 < 0$ and $C_0 + s u_1 > 0$; thus, Eq. (7) becomes

$$P_3 > (P_1 + P_2) \quad (8)$$

In particular, when $P_1 = P_2$, $u_1 = -u_2$, and $u_3 = 0$, the following result can be obtained:

$$P_3 > 2P_1 \quad (9)$$

After the shock waves collide, the intensity of the shock wave produced on the collision surface becomes greater than the sum of the intensities of the two shock waves rather than their simple linear superposition.

Fig. 2 diagrams the shock wave convergence and stacking during the detonation of an explosive from both ends. The total energy (E_T) of the explosive is the sum of the potential energy (E_P) and the kinetic energy (E_K) [22] in terms of energy conservation,

$$E_T = E_P + E_K = \frac{P}{\gamma - 1} + \frac{1}{2} \rho u^2 \quad (10)$$

where γ indicates the adiabatic factor, the first term is the potential energy (pressure energy), and the second term is the

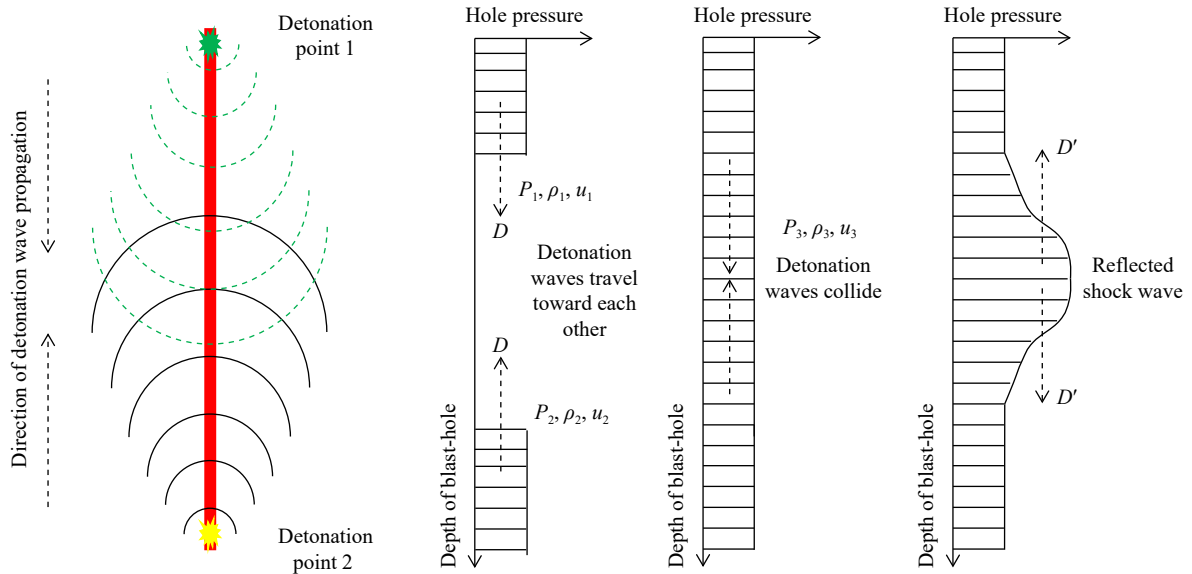


Fig. 2. Shock wave convergence and stacking during detonation from both ends. D —Shock wave convergence; D' —Shock wave stacking.

kinetic energy. Pressure energy is beneficial for improving rock breaking ability. When two shock waves propagate to each other, the particle velocity on the collision surface is $u_3 = u_1 + u_2 = 0$, and the pressure increases to P_3 . According to the energy conservation equation, the kinetic energy is converted into potential energy with decreasing particle velocity and increasing rock breaking ability.

3. Explosion wave field of the detonation from both ends

3.1. Experimental system and scheme

Fig. 3 displays the high-speed schlieren experiment system used here [23–25]. Its laser generates a group of stable lasers that pass through a beam-expanding mirror, resulting in astigmatism and pass through plane and concave mirrors, generating a group of parallel light fields. The parallel light

fields pass through the plane mirror and reach the high-speed camera through a knife edge. A detonator detonates an explosive, and a synchronous controller controls the detonator in conjunction with a high-speed camera, which shoots at 100000 frames per second. The explosive was dinitrodiazophenol, which was detonated from both ends.

3.2. Propagation of explosion waves and gas

Fig. 4 presents the propagation of the explosion waves and gas produced by the double-end detonated explosive. At $t = 10 \mu s$, a high-voltage electric spark detonates the explosive. Then, two groups of explosion waves propagate in opposite directions, and each detonation wave and the charge axis form a certain angle α .

The explosion shock wave on each side extends radially and axially. At $t = 30 \mu s$, the explosion shock waves and the detonation gas separate, and the explosion energy starts to

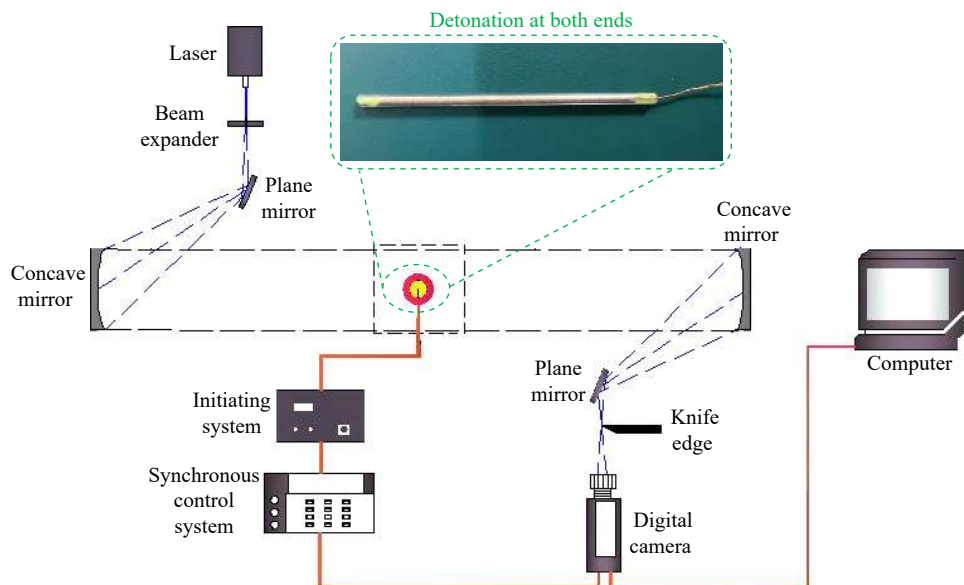


Fig. 3. High-speed schlieren experiment system.

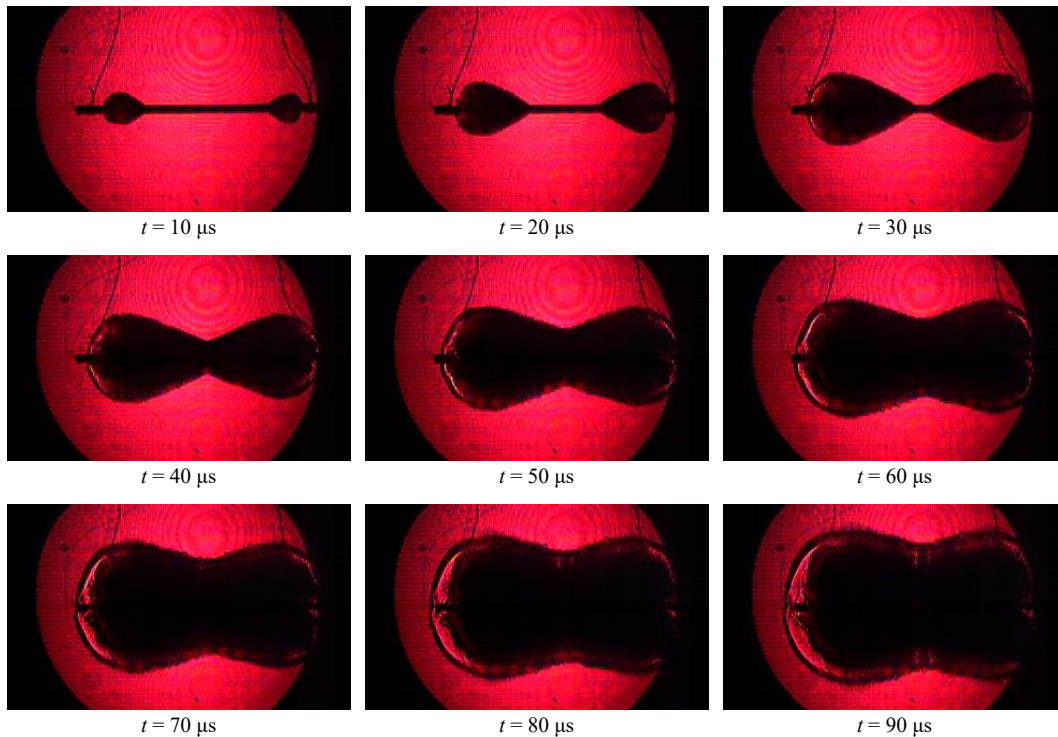


Fig. 4. Propagation of explosion waves and gas from the explosive detonated from both ends. t —Time after detonation.

decay along the axial reverse direction. The axial direction has a higher decay rate than the radial direction. After the collision and superposition of the explosion waves, the superimposed shock wave is dumbbell shaped, which is kept during expansion. At $t = 80 \mu s$, the radial shock waves are separated from the explosion gas, demonstrating the start of the explosion energy decay.

Fig. 5 illustrates the explosion wave velocity. By taking images, the tip of an explosion shock wave can be obtained, and then, the propagation explosion shock wave velocity can be computed.

Fig. 6 is the evolution of the explosion shock wave velocity with time on both-end explosive detonation. At 0–30 μs , the explosion waves on both sides propagate along the charge direction with a propagation velocity of approximately 2500 m/s. During the experiments, the velocity of dinitrodiazophenol was less than the theoretical velocity because it was not compacted in the bulk state. After 30 μs , the explosion waves on both sides collide and superimpose, and the intens-

ity of the superimposed shock wave in the collision region increases. The superimposed shock wave velocity in the collision region is greater than the radial shock wave velocity, which is greater than the axial shock wave velocity. The mean of the explosion wave transmission angles, α , is 60° .

3.3. Stress analysis of the blast hole wall in the superposition area

The two groups of explosion waves transmitted in opposite directions produce a strong-impact shock wave in the collision superposition area, and the superimposed explosion shock wave is linear (Fig. 7). The above analysis indicates that the intensity of the superimposed shock wave on the collision surface is greater than the sum of the intensities of the two shock waves after their frontal collision. The strong superimposed shock wave on the collision surface acts on the blast hole wall, increasing its damage effect.

Fig. 8(a) and (b) displays the interaction between the explosion shock waves and the blast hole wall. The explosion

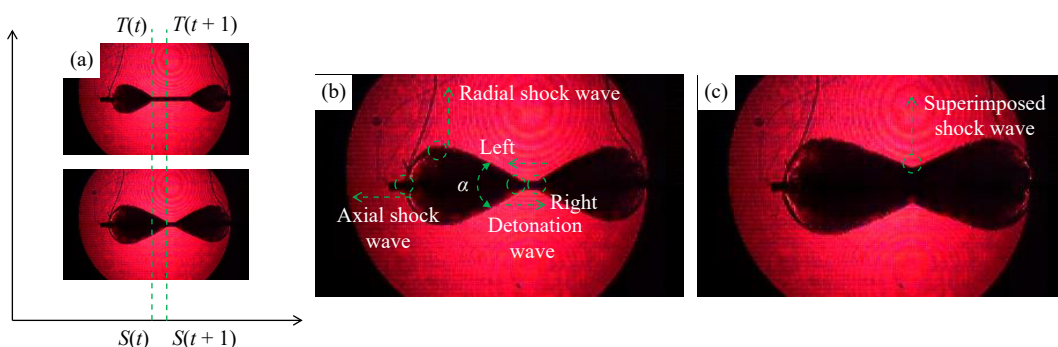


Fig. 5. Schematic of the explosion wave velocity: (a) explosive shock wave position and time images; (b) schematic of the explosion shock wave collision region; (c) schematic of the explosion shock wave superposition region. $S(t)$ —Shock wave position at time t ; $S(t + 1)$ —Shock wave position at time $t + 1$; T —Shock wave position as a function of time.

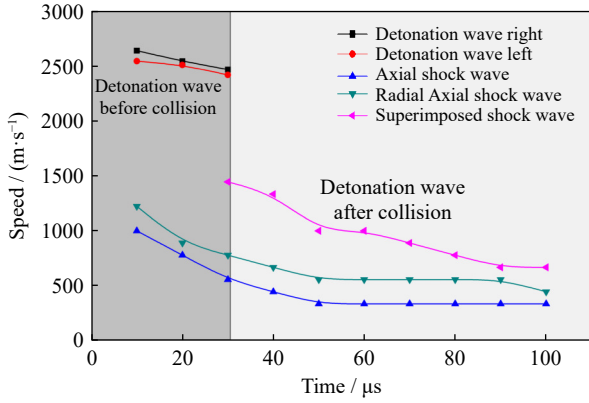


Fig. 6. Explosion shock wave velocity versus time after the detonation of the explosive from both ends.

shock waves are transmitted toward each other at an angle α , and the angle between each explosion shock wave front and the blast hole wall is β . The pressure angle of the blast hole wall under an explosion shock wave is δ .

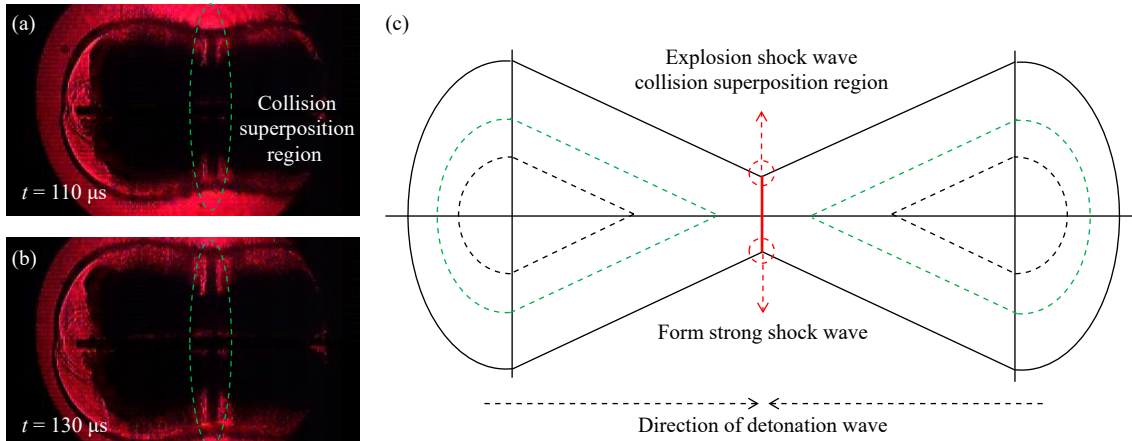


Fig. 7. Schematic of the explosion shock wave collision superposition region on: (a) superimposed shock wave state at 110 μs ; (b) superimposed shock wave state at 130 μs ; (c) shock wave collision superposition schematic.

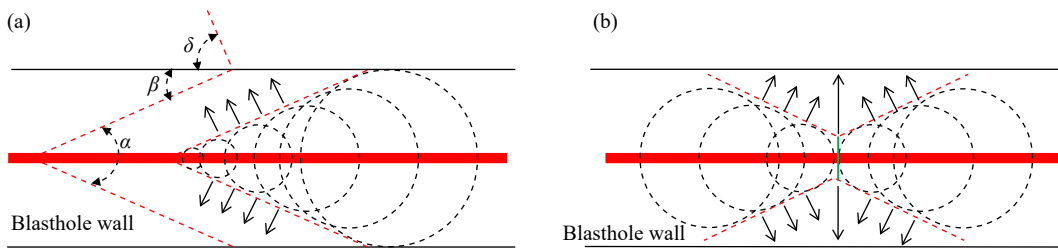


Fig. 8. (a) Interaction between explosion shock waves and the blast hole wall and (b) superimposed shock wave that acts on the blast hole wall.

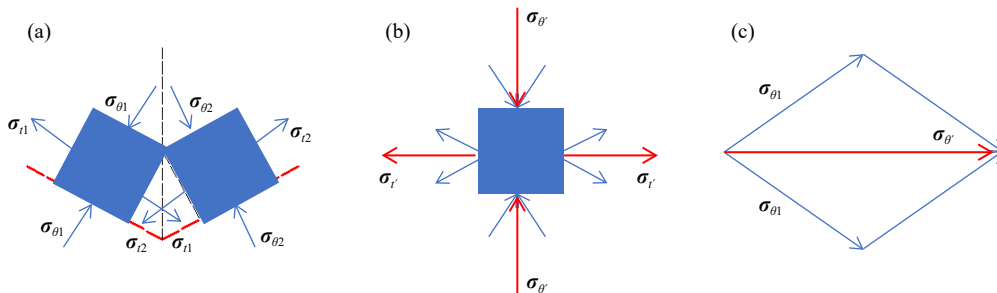


Fig. 9. Stress element of the blast hole wall in the superimposition area: (a) shock wave and blast hole wall stresses from both ends; (b) superimposed shock wave and blast hole wall stresses; (c) stress vector state in the superposition area.

$$\delta = 90^\circ - \beta = 90^\circ + \frac{1}{2}\alpha \tag{11}$$

The explosion waves after the both-end explosive detonation compress in the middle region, producing a 90° incidence angle to the blast hole wall in the superimposed region. The stress element of the blast hole wall in the superimposed area in Fig. 9 is used as an example.

Let σ be the stress state at any point and $\sigma_{\theta 1}$ (compressive stress) and $\sigma_{r 1}$ (tensile stress) be the rightward explosion shock wave and blast hole wall stresses, respectively. Let $\sigma_{\theta 2}$ (compressive stress) and $\sigma_{r 2}$ (tensile stress) be the leftward explosion shock wave and blast hole wall stresses, respectively. Based on the stress superposition, the stress states at the blast hole wall in the final superposition area are $\sigma_{\theta'}$ (compressive stress) and $\sigma_{r'}$ (tensile stress). By vector calculation, the stress states in the superposition area are

$$\begin{cases} \sigma_{\theta'} = \sqrt{|\sigma_{\theta 1}|^2 + |\sigma_{\theta 2}|^2 + 2|\sigma_{\theta 1}||\sigma_{\theta 2}|\cos(\sigma_{\theta 1}, \sigma_{\theta 2})} \\ \sigma_{r'} = \sqrt{|\sigma_{r 1}|^2 + |\sigma_{r 2}|^2 + 2|\sigma_{r 1}||\sigma_{r 2}|\cos(\sigma_{r 1}, \sigma_{r 2})} \end{cases} \tag{12}$$

Due to a single and continuous explosion, theoretically, the forces of the explosion waves on both sides are equal, i.e., $\sigma_{\theta 1} = \sigma_{\theta 2} = \sigma_{\theta}$ and $\sigma_{r 1} = \sigma_{r 2} = \sigma_r$; thus,

$$\begin{cases} \sigma_{\theta'} = \sqrt{|\sigma_{\theta 1}|^2 + |\sigma_{\theta 2}|^2 + 2|\sigma_{\theta 1}||\sigma_{\theta 2}|\cos(\sigma_{\theta 1}, \sigma_{\theta 2})} \\ \sigma_{r'} = \sqrt{|\sigma_{r 1}|^2 + |\sigma_{r 2}|^2 + 2|\sigma_{r 1}||\sigma_{r 2}|\cos(\sigma_{r 1}, \sigma_{r 2})} \end{cases} \quad (13)$$

We take the explosion shock wave propagating to the left in Fig. 10 as an example. This explosion shock wave is incident on the blast hole wall, producing an included angle δ with the blast hole wall. Similarly, the included angle of the explosion shock wave propagating to the right with the blast hole wall is δ .

Furthermore, it can be concluded that

$$\cos(\sigma_{\theta 1}, \sigma_{\theta 2}) = \cos(\pi - 2\delta) = \cos \alpha \quad (14)$$

Substituting Eq. (14) into Eq. (13) obtains the relationship between the superimposed and incident stresses:

$$\begin{cases} \sigma_{\theta'} = \sqrt{2|\sigma_{\theta}|^2 + 2|\sigma_{\theta}|^2 \cos(\sigma_{\theta}, \sigma_{\theta})} = \\ \sqrt{2|\sigma_{\theta}|^2 + 2|\sigma_{\theta}|^2 \cos \alpha} = \sqrt{2 + 2 \cos \alpha} \times \sigma_{\theta} \\ \sigma_{r'} = \sqrt{2|\sigma_r|^2 + 2|\sigma_r|^2 \cos(\sigma_r, \sigma_r)} = \\ \sqrt{2|\sigma_r|^2 + 2|\sigma_r|^2 \cos \alpha} = \sqrt{2 + 2 \cos \alpha} \times \sigma_r \end{cases} \quad (15)$$

where α indicates the included angle of the explosion wave head, i.e., the superimposed and initial stress intensities have a certain coefficient relationship that is associated with the included angle of the explosion wave transmission. In the schlieren experiments, $\alpha = 60^\circ$, $\sigma_{\theta'} = \sqrt{3}\sigma_{\theta}$, and $\sigma_{r'} = \sqrt{3}\sigma_r$.

4. Numerical simulations of the damage distribution in the blast hole wall

4.1. Explosion crack propagation morphology after both-end detonation

It has been revealed that poly(methyl methacrylate)

(PMMA) has similar dynamic fracture characteristics to rock materials under dynamic loading [26–28]. PMMA was employed as an experimental material in the model tests. The model had a length of 400 mm and a width of 300 mm. The cylindrical blast hole had a length of 100 mm and a width of 4 mm. The explosive used was dinitrodiazophenol, and two initiation points were placed at both ends of the charge, as shown in Fig. 11(a).

Fig. 11(b) and (c) presents the experimental results and binarization diagram of an explosion crack. Large-scale radial explosive cracks were generated on the blast hole wall in the superimposed area during both-end explosive detonation, and the crack widths in the radial fracture expansion area were different. The explosive crack width in the strong-impact region was approximately 3 times that in the weak-impact region, approximately 11 times the blast hole diameter, and approximately 5% of the blast hole length. From Fig. 12, this difference is because the explosion products superimpose and form a wide fracture zone in the fracture region of the strong-impact loading region. With the reduction of the superimposed stress and under the action of the explosion gas wedge, the explosion crack width is reduced.

4.2. Numerical simulations of the explosion crack propagation

LS-DYNA, a finite element numerical simulation software program, was employed to develop a test model in a 1:1 ratio. Because of the large deformation and displacement in the simulation of an explosion problem, to avoid calculation failure resulting from grid distortion, we employ the arbitrary Lagrange–Euler algorithm. The Euler algorithm was employed for the explosive, which was simulated using the *MAT_HIGH_EXPLOSIVE_BURN keyword. The Jones–Wilkins–Lee equation of state was applied to simulate the

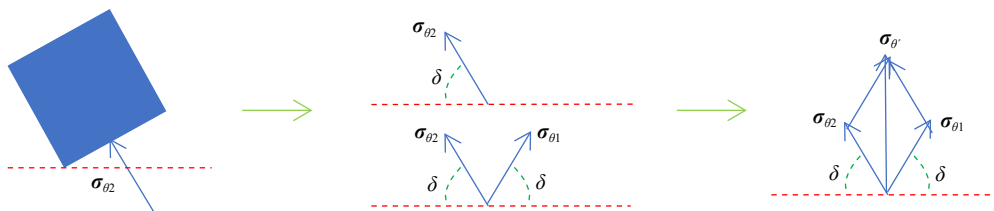


Fig. 10. Stacking stress calculation.

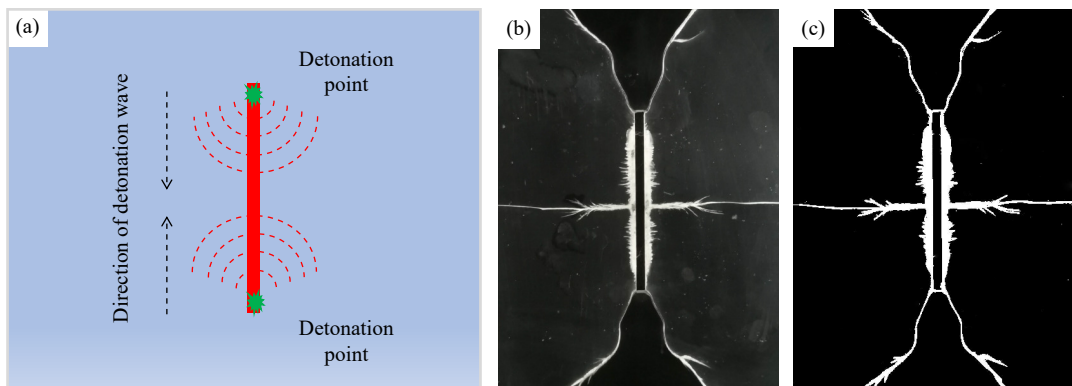


Fig. 11. Explosion experimental after both-end detonation: (a) experimental model; (b) experimental results; (c) crack binarization diagram.

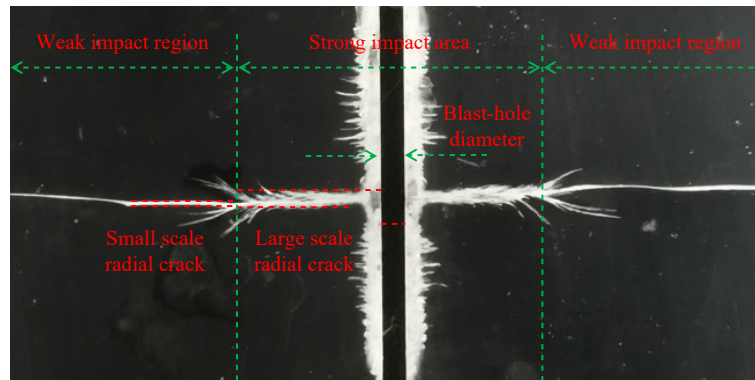


Fig. 12. Large-scale radial crack rupture form.

pressure–volume relationship in the explosion process [29]:

$$P = A \left(1 - \frac{\varpi}{R_1}\right) e^{-R_1 V} + B \left(1 - \frac{\varpi}{R_2}\right) e^{-R_2 V} + \frac{\varpi E_0}{V} \quad (16)$$

where P indicates the pressure, V indicates the relative volume, R_1 , R_2 , A , B , and ϖ indicate the constants, i.e., $R_1 = 4.8$, $R_2 = 1.2$, $\varpi = 0.3$, $A = 405$ GPa, and $B = 0.43$ GPa, and E_0 is the initial internal energy density.

Herein, PMMA and organic glass were simulated using the *MAT_JOHNSON_HOLMQUIST_CERAMICS keyword and the Lagrange algorithm, respectively. In the *MAT_JOHNSON_HOLMQUIST_CERAMICS material model, D is the cumulative damage and primarily the plastic strain accumulation [30–31].

$$D = \sum \frac{\Delta \varepsilon^p}{\Delta \varepsilon_f^p} \quad (17)$$

where $\Delta \varepsilon^p$ refers to the accumulated plastic strain in the loading process and $\Delta \varepsilon_f^p$ refers to the plastic strain during fracture under pressure P . Plexiglass plate has parameters of density $\rho = 2.53 \text{ g}\cdot\text{cm}^{-3}$, shear modulus $G = 0.304$ GPa, complete strength parameter $A = 0.93$, crack strength parameter $B = 0.088$, fracture strength parameter $M = 0.35$, strength index $N = 0.77$, elastic limit $H_{EL} = 0.0595$ GPa, strain rate $C = 0.03$, and failure criterion $F_s = 0.8$.

HYPERMESH preprocessing software was employed for model establishment, mesh division, algorithm definition, and boundary condition setting, as presented in Fig. 13. Quadrilateral (quads) and triangular (trias) elements were employed to divide the grid into front units. Different detonation points were set based on the coordinate position using the *INITIAL_DETONATION keyword.

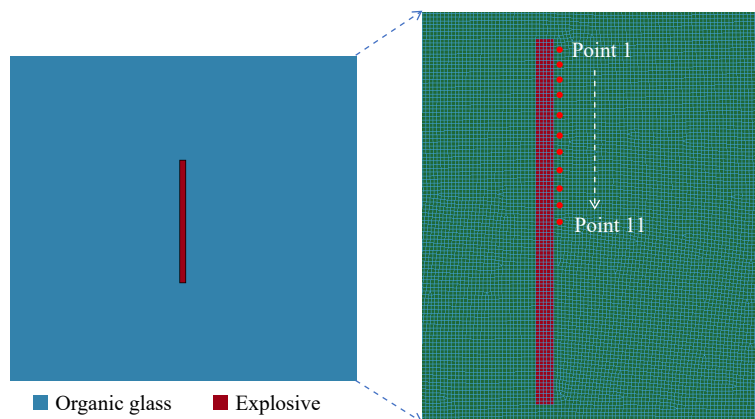


Fig. 13. Schematic of the model and mesh division of the both-end explosive detonation.

Fig. 14 illustrates the Mises equivalent stress propagation process during both-end explosive detonation. In the stress cloud diagram, the stress field intensities shown in red, green, and blue successively decrease. The Mises stress waveform is triangular before the superimposed collision and extends primarily along the charge section and radial directions. At $t = 10 \mu\text{s}$, the effective stresses superpose in the middle of the blast hole, and the stress intensity on superposition reaches a maximum. At $t = 15 \mu\text{s}$, an effective stress with a higher intensity is observed in the superposition area, which presents a rhomboid expansion mode and finally produces an oval distribution.

Fig. 15 presents the medium damage around the blast hole. The red and green areas indicate the crushing and crack areas, respectively. The numerical simulation results align with the model experimental results and demonstrate that large-scale radial explosive cracks are produced in the central superimposed area. Before $10 \mu\text{s}$, with the detonation transfer, an outstanding crushing zone is found around the blast hole under the strong explosive dynamic load, and explosive cracks start to emerge at the end of the blast hole. At $t = 10 \mu\text{s}$, explosive cracks start to emerge in the superposition region. Due to the strong dynamic loading resulting from the superposition, the crack size is large at the start of the su-

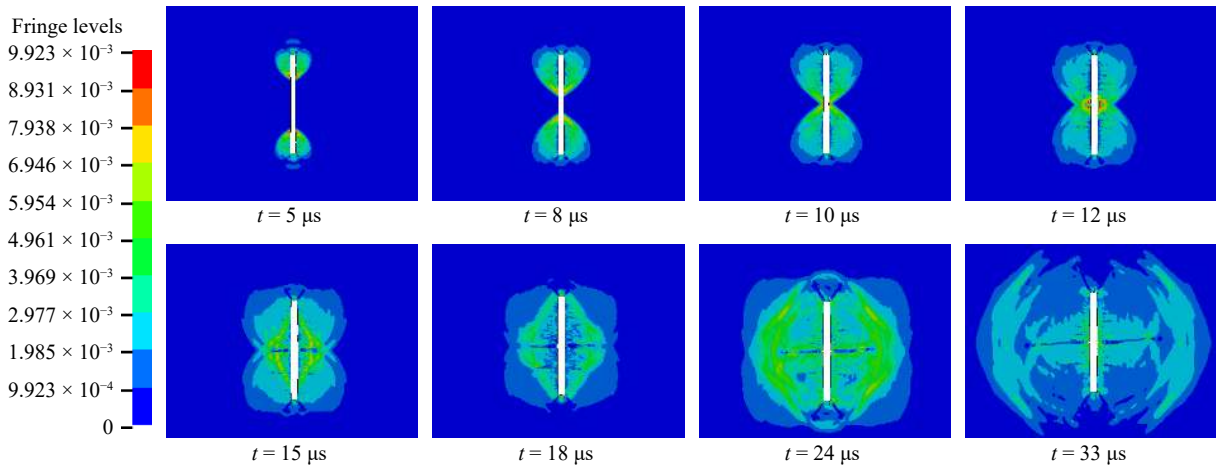


Fig. 14. Mises equivalent stress propagation process.

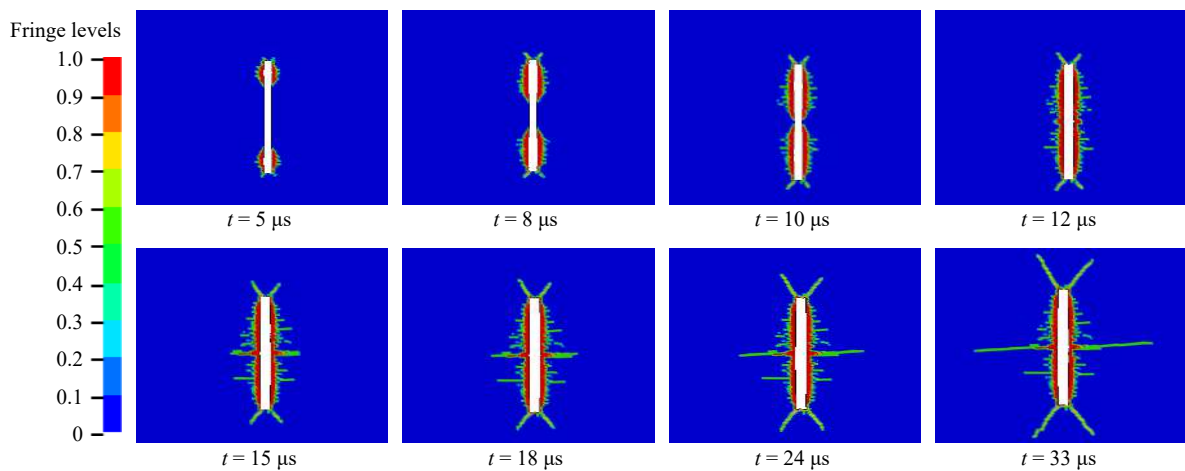


Fig. 15. Medium damage around the blast hole.

perposition, which aligns with the model test results. After 24 μs, the crack propagation width in the superimposed region decreases because of stress attenuation in the superimposed region.

On the basis of the model test and numerical simulation results, large-scale radial cracks are generated in the superimposed area, as depicted in Fig. 16. With the initiation of superimposed cracks on the blast hole wall, crack propagation shows a change from wide to narrow cracks. This is caused by the strong dynamic loading on superposition, which forms a strong-impact region in a certain area of the blast hole wall, resulting in the instantaneous destruction of the medium in that area and the formation of a large-width crack. Then, due to the attenuation of the explosion, an excessive crack area is produced, and the crack propagation width is reduced.

Fig. 17(a) presents the arrangement of the measuring points on the blast hole wall along the axial direction. Considering the explosion distribution symmetry during both-end explosive detonation, the measuring points are set from one end of the blast hole at 5-mm intervals, with the first point being measuring point 1 and the collision position in the middle being measuring point 11. Fig. 17(b) displays the pressure distribution of the blast hole wall along the axial direction. The peak pressure value of each measurement point was extracted. After the detonation at the initiation points, each peak

pressure value at the blast hole wall quickly increases and then gradually stabilizes with the propagation of the explosion stress waves. At each detonation point, the blast hole wall pressure is the minimum, and the peak pressure is 190 MPa. In contrast, the blast hole wall pressure is the maximum, and the peak pressure is 540 MPa at the charge center. The pressure in the central superposition area is approxim-

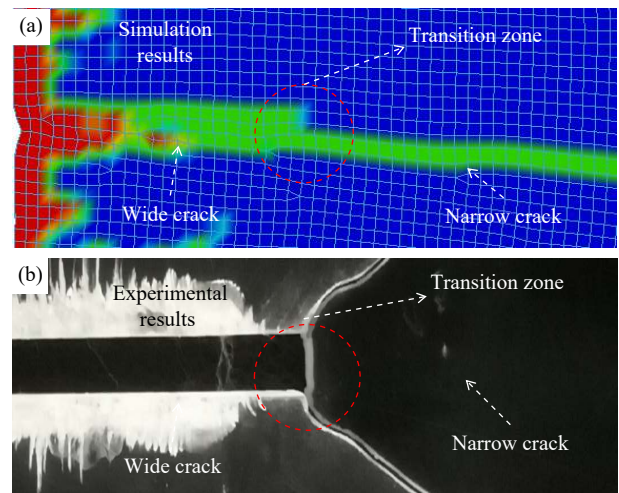


Fig. 16. Large-scale radial crack propagation based on (a) numerical simulation and (b) model test results.

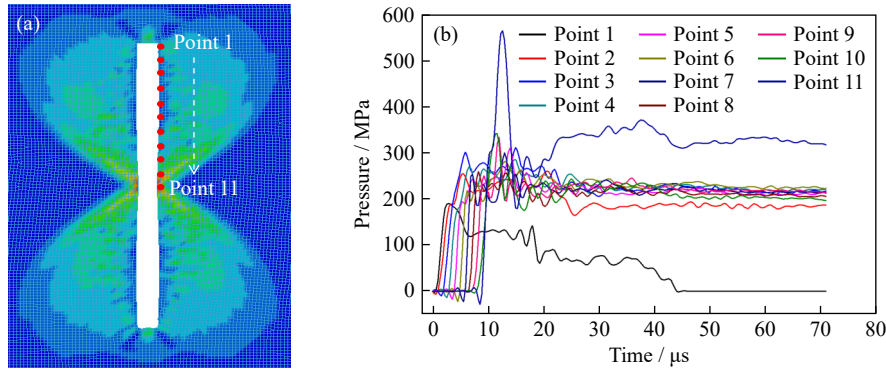


Fig. 17. (a) Measuring point locations and (b) blast hole wall pressure distribution along the axial direction.

ately 2.84 times greater than that at the initiation ends.

To more accurately examine the pressure of the blast hole wall in the superposition area, four measuring points were arranged between measuring points 10 (corresponding to 45 mm of charge) and 11 (corresponding to 50 mm of charge) (Fig. 18(a)). The extracted pressure curve of the blast hole wall in this section is displayed in Fig. 18(b). The blast hole wall pressure gradually increases with a decrease in distance from the measuring point to the center. The superposition area of the blast hole wall is significantly improved in the center 5-mm range, accounting for 5% of the total charge length.

The points around the blast hole at which the peak pressure is extracted are depicted in Fig. 19(a), and the fitted peak pressure–blast hole length relationship is presented in Fig. 19(b). The distribution of the pressure shows a valley pattern, and the distribution characteristics of the peak pressure of the foundation are divided into three areas: nonsuperimposed, weakly superimposed, and strongly superimposed areas, which account for 80%, 15%, and 5% of charge length, respectively. The average peak pressures are 274, 341, and 504 MPa, respectively. The mean peak pressures in the strongly superimposed area are 1.48 and 1.84 times greater than those in the weakly superimposed and nonsuperimposed areas, respectively.

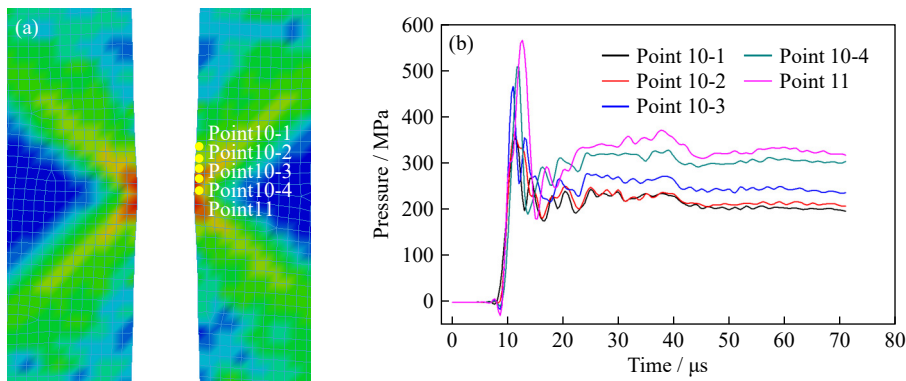


Fig. 18. (a) Additional measuring point locations and (b) blast hole wall pressure distribution near the superposition area.

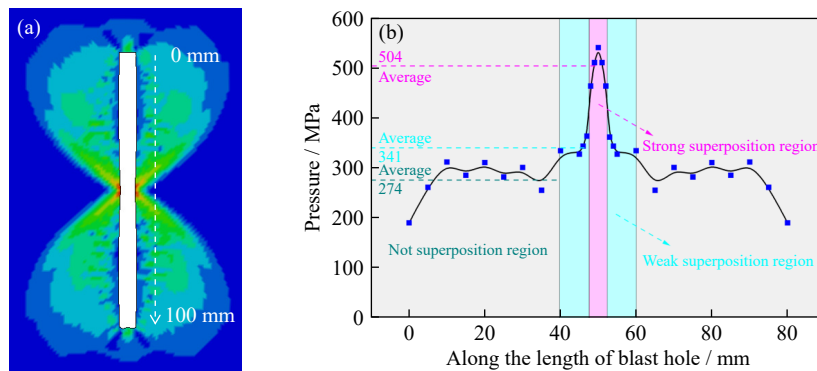


Fig. 19. (a) Range of pressure measuring points and (b) variation curve of peak pressure along the length of the blast hole.

5. Conclusions

This work aims to explore the explosion wave field and rock breaking effect of the two ends of the detonated explos-

ive in a blast hole in terms of shock wave collision, stress change of the hole wall in the collision zone, and crack propagation in the collision zone.

(1) The intensity of the superimposed shock wave on the

collision surface was greater than the sum of the intensities of the colliding shock waves. At the collision site, the kinetic energy was transformed into potential energy with a decrease in particle velocity on the wave front, and the wave front pressure increased.

(2) The expansion form of the superimposed shock wave was dumbbell shaped, and when the two shock waves collided and superimposed, the intensity in the collision area rose. The shock wave velocity in the collision area was greater than the radial shock wave velocity, and the average propagation angle of the explosion shock waves was approximately 60°.

(3) A stress model of the blast hole wall in the superimposed area was established. A fitted relationship between blast hole wall stress and explosion wave propagation angle in the superimposed area was plotted. Under the experimental conditions, the superimposed stress of the blast hole wall was approximately 1.73 times the single-explosion wave incident stress.

(4) The results of the model test and numerical simulations revealed that large-scale radial fracture cracks were produced on the blast hole wall in the superimposed area. The width of the large-scale radial fracture cracks resulting from the strong impact was approximately 5% of the blast hole length. The mean peak pressures in the strongly superimposed area were approximately 1.48 and 1.84 times greater than those in the weakly superimposed and nonsuperimposed areas, respectively.

Acknowledgements

This research was financially supported by the National Natural Science Foundation of China (Nos. 52208384 and 51934001), the National Key Research and Development Program of China (No. 2021YFB3401501), the State Key Laboratory of Precision Blasting and Hubei Key Laboratory of Blasting Engineering, Jiangnan University (No. PBSKL2022C05).

Conflict of Interest

Renshu Yang is an advisory board member for this journal and was not involved in the editorial review or the decision to publish this article. The authors declared that they have no conflicts of interest in this work.

References

- [1] Z.D. Leng, J.S. Sun, W.B. Lu, *et al.*, Mechanism of the in-hole detonation wave interactions in dual initiation with electronic detonators in bench blasting operation, *Comput. Geotech.*, 129(2021), art. No. 103873.
- [2] L.B. Jayasinghe, H.Y. Zhou, A.T.C. Goh, Z.Y. Zhao, and Y.L. Gui, Pile response subjected to rock blasting induced ground vibration near soil-rock interface, *Comput. Geotech.*, 82(2017), p. 1.
- [3] R.P. Dhakal and T.C. Pan, Response characteristics of structures subjected to blasting-induced ground motion, *Int. J. Im-*
- pact Eng.*, 28(2003), No. 8, p. 813.
- [4] C.Q. Wu, H. Hao, and Y. Lu, Dynamic response and damage analysis of masonry structures and masonry infilled RC frames to blast ground motion, *Eng. Struct.*, 27(2005), No. 3, p. 323.
- [5] Z.X. Zhang, D.F. Hou, and A. Aladejare, Empirical equations between characteristic impedance and mechanical properties of rocks, *J. Rock Mech. Geotech. Eng.*, 12(2020), No. 5, p. 975.
- [6] Z.X. Zhang, Effect of double-primer placement on rock fracture and ore recovery, *Int. J. Rock Mech. Min. Sci.*, 71(2014), p. 208.
- [7] Q.B. Zhang, Z.X. Zhang, C.S. Wu, J.S. Yang, and Z.Y. Wang, Characteristics of vibration waves measured in concrete lining of excavated tunnel during blasting in adjacent tunnel, *Coatings*, 12(2022), No. 7, art. No. 954.
- [8] Z.D. Leng, W.B. Lu, M. Chen, Y. Fan, P. Yan, and G.H. Wang, Explosion energy transmission under side initiation and its effect on rock fragmentation, *Int. J. Rock Mech. Min. Sci.*, 86(2016), p. 245.
- [9] Z.D. Leng, Y. Fan, W.B. Lu, Q.D. Gao, and J.R. Zhou, Explosion energy transmission and rock-breaking effect of in-hole dual initiation, *Chin. J. Rock Mech. Eng.*, 38(2019), No. 12, p. 2451.
- [10] I.A. Onederra, J.K. Furtney, E. Sellers, and S. Iverson, Modeling blast induced damage from a fully coupled explosive charge, *Int. J. Rock Mech. Min. Sci.*, 58(2013), p. 73.
- [11] L. Liu, M. Chen, W.B. Lu, Y.G. Hu, and Z.D. Leng, Effect of the location of the detonation initiation point for bench blasting, *Shock. Vib.*, 2015(2015), art. No. 907310.
- [12] Q.D. Gao, W.B. Lu, P. Yan, H.R. Hu, Z.W. Yang, and M. Chen, Effect of initiation location on distribution and utilization of explosion energy during rock blasting, *Bull. Eng. Geol. Environ.*, 78(2019), No. 5, p. 3433.
- [13] Q.D. Gao, W.B. Lu, Z.D. Leng, Z.W. Yang, Y.Z. Zhang, and H.R. Hu, Effect of initiation location within blasthole on blast vibration field and its mechanism, *Shock. Vib.*, 2019(2019), art. No. 5386014.
- [14] Y.S. Miao, X.J. Li, H.H. Yan, X.H. Wang, and J.P. Sun, Experimental study of bilinear initiating system based on hard rock pile blasting, *Shock. Vib.*, 2017(2017), art. No. 3638150.
- [15] Y.S. Miao, X.J. Li, H.H. Yan, X.H. Wang, and J.P. Sun, Research and application of a symmetric bilinear initiation system in rock blasting, *Int. J. Rock Mech. Min. Sci.*, 102(2018), p. 52.
- [16] H. Haeri, Experimental and numerical study on crack propagation in pre-cracked beam specimens under three-point bending, *J. Cent. South Univ.*, 23(2016), No. 2, p. 430.
- [17] J.J. Zuo, R.S. Yang, X.M. Ma, L.Y. Yang, and Y. Zhao, Explosion wave and explosion fracture characteristics of cylindrical charges, *Int. J. Rock Mech. Min. Sci.*, 135(2020), art. No. 104501.
- [18] J.J. Zuo, R.S. Yang, M. Gong, and P. Xu, Explosion wave and crack field of an eccentric decoupled charge, *Appl. Optics.*, 60(2021), No. 33, p. 10453.
- [19] R.S. Yang and J.J. Zuo, Experimental study on directional fracture blasting of cutting seam cartridge, *Shock. Vib.*, 2019(2019), art. No. 1085921.
- [20] S.I. Gerasimov and N.A. Trepalov, Background oriented schlieren method as an optical method to study shock waves, *Tech. Phys.*, 62(2017), No. 12, p. 1799.
- [21] J.J. Ding, J.H. Yang, Z.W. Ye, Z.D. Leng, C. Yao, and C.B. Zhou, Cut-blasting method selection and parameter optimization for rock masses under high in situ stress, *Int. J. Geomech.*, 23(2023), No. 12, art. No. 04023211.
- [22] S.C. Lin, Cylindrical shock waves produced by instantaneous energy release, *J. Appl. Phys.*, 25(1954), No. 1, p. 54.
- [23] K. Wang, Z.Q. Shi, Y.J. Shi, Z.G. Zhao, and D. Zhang, Characteristics of electrical explosion of single wire in a vacuum and in the air, *Acta Phys. Sin.*, 66(2017), No. 18, art. No. 185203.
- [24] K. Wang, Z.Q. Shi, Y.J. Shi, and Z.G. Zhao, Characteristics of

- the electrical explosion of fine metallic wires in vacuum, *AIP Adv.*, 7(2017), No. 9, art. No. 095002.
- [25] L.C. Forde, W.G. Proud, S.M. Walley, P.D. Church, and I.G. Cullis. Ballistic impact studies of a borosilicate glass, *Int. J. Impact. Eng.*, 37(2010), No. 5, p. 568.
- [26] M.R. Ayatollahi, A.R. Torabi, and M. Firoozabadi, Theoretical and experimental investigation of brittle fracture in V-notched PMMA specimens under compressive loading, *Eng. Fract. Mech.*, 135(2015), p. 187.
- [27] R. Zhang, R. Guo, and S.Y. Wang, Mixed mode fracture study of PMMA using digital gradient sensing method, *Eng. Fract. Mech.*, 119(2014), No. 2, p. 164.
- [28] W. Xu, X.F. Yao, H.Y. Yeh, and G.C. Jin, Fracture investigation of PMMA specimen using coherent gradient sensing (CGS) technology, *Polym. Test.*, 24(2005), No. 7, p. 900.
- [29] Y.B. Wang, Z.J. Wen, G.Q. Liu, *et al.*, Explosion propagation and characteristics of rock damage in decoupled charge blasting based on computed tomography scanning, *Int. J. Rock Mech. Min. Sci.*, 136(2020), art. No. 104540.
- [30] T.W. Dong, H.S. Liu, S.L. Jiang, *et al.*, Simulation of free surface flow with a revolving moving boundary for screw extrusion using smoothed particle hydrodynamics, *Comput. Model. Eng. Sci.*, 95(2013), No. 5, p. 369.
- [31] Z.L. Wang, H.C. Wang, J.G. Wang, and N.C. Tian, Finite element analyses of constitutive models performance in the simulation of blast-induced rock cracks, *Comput. Geotech.*, 135(2021), art. No. 104172.